Daily calibration of the fluxgate magnetometer onboard the Cluster spacecraft

N. Grimmich[1], H.U. Auster[1], C. Carr[3], O.D. Constantinescu[1,2], K.H. Fornaçon[1], K.H. Glassmeier[1], and F. Plaschke[1]

[1]Institute for Geophysics and Extraterrestrial Physics, TU Braunschweig, Germany
[2]Institute for Space Sciences, Bucharest, Romania
[3]Imperial College London, London, United Kingdom

January 22, 2026

During their 24 years mission of investigating the Earth's magnetosphere the four Cluster satellites delivered high quality magnetic field data measured by the onboard fluxgate magnetometers. To achieve the accuracy required for scientific studies, the raw magnetic field data need to be calibrated on a regular basis. We briefly review the methods used for the Cluster in-flight magnetic field data calibration and present a statistical analysis of the calibration parameters and their long-term trends. This work aims to serve as a guide for researchers using the Cluster FGM data in the future, as well as a general reference for long-term behaviour of the calibration parameters of fluxgate magnetometers.

1 Introduction

The Cluster mission (Escoubet et al., 1997), launched by the European Space Agency (ESA) in 2000, was the first mission to study the near-Earth space environment using four identical satellites. The mission aimed to study three-dimensional structures and macroscopic turbulence in the Earth space plasma environment. Each of the four Cluster spacecraft was equipped with eleven scientific instruments delivering multipoint fields and particle measurements. The tetrahedral flight formation of the four spacecraft

enabled the separation of the spatial and temporal fluctuations in key regions of the Earth's plasma environment (Escoubet et al., 2021).

One of the key measurements delivered by Cluster was the magnetic field vector, measured by the fluxgate magnetometer (FGM) experiment (Balogh et al., 1997). Fluxgate magnetometers use coils wounded around a ferromagnetic core, one coil periodically drives the core in and out of saturation, while the second one picks up the signal to be measured (Primdahl, 1979). Because the relative permeability varies with the intensity of the magnetic field, a strong non-linear coupling results in harmonics of the driven frequency in the pick-up coil. The amplitude of the even harmonics is proportional with the magnitude of the magnetic field component parallel to the core, enabling very precise measurement of the vector magnetic field.

The Cluster FGM experiment consists of eight tri-axial fluxgate sensors and the associated electronics units onboard the four Cluster spacecraft. Each spacecraft accommodates a pair of tri-axial sensors on a 5.2 m long radial boom lying in the spin-plane. The outboard sensor triad is placed at the end of the boom, while the other triad is placed 1.5 m inboard from the boom end. The data provided by the FGM was measured by the outboard sensor. The inboard sensor was intended as backup in case of the outboard sensor malfunction. Measurements from the inboard sensor were also necessary for checking – and eventually correcting – potential artificial disturbances generated by other instruments onboard or by spacecraft subsystems. Since all outboard sensors performed flawlessly and no artificial disturbances were observed in the data, using the inboard sensor data was not necessary.

To cover a wide range of magnetic field strengths (from 1 nT in the solar wind and distant lobes to over 10 000 nT close to the perigee) the instruments automatically switch between six ranges with different digital resolutions, as shown in Table 1. The digital resolution spanned from 7.8 pT for the lowest range to 8 nT for the highest. Of the six ranges used for in-flight data acquisition, ranges 6 and 7 were not initially intended for use during the nominal mission. They were designed solely for ground testing. However, as the mission progressed, particularly during the second half of the mission when the orbits were slowly lowered, these ranges were used more frequently. One of two Analog to Digital Converters (ADC) can be selected to translate the measurements from voltages to digital units.

Other instruments onboard rely on the value of the ambient magnetic field vector provided by the FGM instrument for their own data processing and calibration. The daily FGM calibration assures that valid magnetic field data is available timely.

The FGM calibration is the process of conversion of the raw digital output from a triad of sensor coils aligned along nonorthogonal axes into magnetic field vectors expressed in physical units in an orthogonal frame with a known orientation with respect to the spacecraft. This transformation is dependent on a number of parameters encoding scaling factors, sensors offsets, orientation, and nonorthogonality. In total there are 12 calibration parameters for each sensor triad and each measurement range. Since Cluster FGM uses 6 ranges, there are in total $2 \times 4 \times 6 \times 12 = 576$ parameters needed for the Cluster FGM calibration. These parameters were determined on ground before launch. Most of these parameters change in time, many of them from day to day. It is therefore

Table 1: Cluster FGM instrument ranges.

range	B_{max} (nT)	resolution (nT)	in operation since
2	64	1/128	2000
3	256	1/32	2000
4	1024	1/8	2000
5	4096	1/2	2006
6	16384	2	2009
7	65536	8	2009

necessary to determine a subset of the calibration parameters on a daily basis. Because routine daily calibration is only carried out for the outboard sensors the number of needed parameters is reduced to half. Over the course of the mission, over 35 000 calibration files, each containing the parameters for one day for the outboard sensor of one spacecraft were produced.

This paper aims to provide an overview of the techniques used for the Cluster FGM in-flight calibration, introduce the dedicated FGM calibration procedure, and discuss the long-term behaviour of the instruments.

2 In-flight magnetometer calibration

The production of calibrated magnetic field data involves two separate major steps: First, the calibration parameters need to be determined based on pre-flight ground measurements and on analysis of the in-flight data, then the estimated parameters must be used to calibrate the data.

2.1 The calibration equation

Let $(\hat{\mathbf{S}}_1, \hat{\mathbf{S}}_2, \hat{\mathbf{S}}_3)$ denote the unit vectors of the sensor coils axes. They define a spinning, nearly orthogonal sensor system roughly aligned with an orthogonal frame $(\hat{\mathbf{x}}, \hat{\mathbf{y}}, \hat{\mathbf{z}})$ rigidly fixed to the sensor triad. Given a magnetic field vector $\mathbf{B}$ in the $(\hat{\mathbf{x}}, \hat{\mathbf{y}}, \hat{\mathbf{z}})$ frame, the sensor j will measure the projection of $\mathbf{B}$ on the sensor's axis $\hat{\mathbf{S}}_j$, affected by the the sensor's gain G_j and offset O_j:

$$B'_j = G_j \hat{\mathbf{S}}_j \cdot \mathbf{B} + O_j \,. \tag{1}$$

Following the existent Cluster FGM calibration software choice of an orthogonal sensor frame with the x-axis aligned with the spacecraft spin, the components of $\hat{\mathbf{S}}_j$ in the orthogonal frame are:

$$\hat{\mathbf{S}}_j = (\cos\theta_j, \sin\theta_j \cos\varphi_j, \sin\theta_j \sin\varphi_j) \,. \tag{2}$$

The elevation angles θ_j are measured with respect to the spin axis. The azimuth angles φ_j are measured with respect to the y-axis in the spin plane, positive towards the z-axis (i.e. positive in the direction of spin rotation).

Eq.(1) can be written in matrix form as

$$\mathbf{B}' = \mathcal{T}\mathbf{B} + \mathbf{O} \tag{3}$$

which is the inverse calibration equation. The transformation matrix $\mathcal{T} = \mathcal{T}_{\rm gain}\mathcal{T}_{\rm ortho}$ is:

$$\mathcal{T} = \begin{pmatrix} G_x & 0 & 0 \\ 0 & G_y & 0 \\ 0 & 0 & G_z \end{pmatrix} \begin{pmatrix} \cos\theta_x & \sin\theta_x\cos\varphi_x & \sin\theta_x\sin\varphi_x \\ \cos\theta_y & \sin\theta_y\cos\varphi_y & \sin\theta_y\sin\varphi_y \\ \cos\theta_z & \sin\theta_z\cos\varphi_z & \sin\theta_z\sin\varphi_z \end{pmatrix} . \tag{4}$$

Because the deviation from orthogonality is small, $\theta_x \approx 0$ and $\varphi_y \approx 0$. It is advantageous to do the following change of variables: $\theta_y \to \pi/2 - \theta_y \approx 0$; $\theta_z \to \pi/2 - \theta_z \approx 0$; $\varphi_z \to \pi/2 - \varphi_z \approx 0$. In addition we introduce the following notations:

$$\begin{array}{lll} \Delta G_{yz} & = G_y - G_z & \approx 0 \quad \text{spin plane gain mismatch} \\ \Delta\varphi_{yz} & = \varphi_y - \varphi_z & \approx 0 \quad \text{spin plane nonorthogonality} \end{array} \tag{5}$$

In practice the digital units from the Analog to Digital Converters (ADC) are already transformed to nominal nT using ground determined parameters before $\mathbf{B}$ is introduced in Eq.(3), therefore the gains are close to unity ($G_j = 1 + \epsilon_j$). With this in mind, the first order approximation of the transformation matrix is

$$\mathcal{T} = \begin{pmatrix} G_x & \theta_x\cos\varphi_x & \theta_x\sin\varphi_x \\ \theta_y & G_y & \varphi_y \\ \theta_z & \varphi_y - \Delta\varphi_{yz} & G_y - \Delta G_{yz} \end{pmatrix} . \tag{6}$$

which is the equivalent of the matrix in Eq.(8) of Kepko et al. (1996).

The calibration equation associated to Eq.(3) is

$$\mathbf{B} = \mathcal{M}(\mathbf{B}' - \mathbf{O}) , \tag{7}$$

where the calibration matrix $\mathcal{M}$ is equal to $\mathcal{T}^{-1}$. In the first order, the calibration matrix is:

$$\begin{aligned} \mathcal{M} &= \begin{pmatrix} 1 & \theta_x\cos\varphi_x & \theta_x\sin\varphi_x \\ \theta_y & 1 & \varphi_y \\ \theta_z & \varphi_y - \Delta\varphi_{yz} & 1 \end{pmatrix}^{-1} \begin{pmatrix} G_x & 0 & 0 \\ 0 & G_y & 0 \\ 0 & 0 & G_y - \Delta G_{yz} \end{pmatrix}^{-1} \\ &= \begin{pmatrix} 1/G_x & -\theta_x\cos\varphi_x & -\theta_x\sin\varphi_x \\ -\theta_y & 1/G_y & -\varphi_y \\ -\theta_z & -(\varphi_y - \Delta\varphi_{yz}) & 1/(G_y - \Delta G_{yz}) \end{pmatrix} . \end{aligned} \tag{8}$$

Eq.(7) in the first order is the basis for both determining the calibration parameters and for the production of calibrated data.

2.2 Determination of the calibration parameters

In-flight calibration consists in determining calibration parameters, i.e., the elements of the transformation matrix $\mathcal{M}$ and of the offset vector $\mathbf{O}$, in total 12 values. In the ideal case when all gains are equal to one and all sensor coils axes are perfectly aligned with the orthogonal frame axes, the transformation matrix is the unit matrix. Incorrect values of some calibration parameters lead to clear coherent signals at spin and double spin frequency in the calibrated magnetic field (Farrell et al., 1995; Kepko et al., 1996; Auster et al., 2002; Plaschke et al., 2019). Other parameters, if assigned incorrect values lead to flawed measurements contradicting known properties of physical phenomena such as the incompressible nature of Alfvén waves in the solar wind (Belcher, 1973; Hedgecock, 1975; Leinweber et al., 2008) or the compressible nature of mirror mode waves in the magnetosheath (Plaschke and Narita, 2016). These are the keys to adjust the calibration parameters to their correct values.

2.3 Specific implementation for Cluster FGM

There are several relevant reference systems for the Cluster FGM in-flight calibration:

SMB - The Spacecraft Mechanical Build system is fixed to the spacecraft body with the x_{SMB}-axis defined by the nominal spin axis. The z_{SMB}-axis leads the y_{SMB}-axis in the direction of rotation.

FS - The nonorthogonal FGM Sensor system is defined by the three sensor coil axes and is roughly aligned with the SMB system. The measurements are made in this system.

OS - The Orthogonalized Sensor system shares the x-axis with the FS system. The y_{OS} is orthogonal to the x_{OS} in the $(x_{\mathrm{FS}}, y_{\mathrm{FS}})$-plane, and z_{OS} completes the system.

FSR - The FGM Spin Reference system has the x_{FSR}-axis defined by the maximum principal inertia axis. The y_{FSR} and z_{FSR} complete the right-handed orthogonal system roughly aligned with the SMB system.

More information about the reference frames used for the FGM data processing can be found in the FGM Data Processing Handbook (FGMDP, Fornaçon et al., 2011).

The transformation from the digital units produced by the ADC to nominal nT in the FS system involves range-dependent, ADC-characteristic scaling matrices and offsets:

$$\mathbf{B}^{\mathrm{FS}} = \mathcal{M}^{(r)}_{\mathrm{scale}}(\mathbf{D} - \mathbf{O}^{(r)}_{\mathrm{ADC}}) \,. \tag{9}$$

The superscript $^{(r)}$ denotes range dependence. The scaling matrices and the ADC offsets were determined during ground calibration campaigns at the TU-Braunschweig Magnetsrode facility (Glassmeier et al., 2007) and are not subject to be changed by the in-flight calibration.

The in-flight calibration takes the magnetic field resulted from Eq.(9) as starting point and computes the calibrated magnetic field in the FSR system.

$$\mathbf{B}^{\mathrm{FSR}} = \mathcal{M}_{\mathrm{rot}}\mathcal{M}_{\mathrm{sc}}\Big(\mathcal{M}_{\mathrm{cal}}^{(r)}(\mathbf{B}^{\mathrm{FS}} - \mathbf{O}^{(r)}) - \mathbf{O}^{\mathrm{sc}}\Big) \tag{10}$$

There are two nested calibrations in Eq. (10): First a range specific (inner) calibration is applied to the magnetic field in the nonorthogonal FS system, resulting in an intermediate range-calibrated magnetic field in the OS system. The range-specific parameters are related the orthogonality and to the electronics and do not arise from real physical magnetic fields. The artificial magnetic fields generated by the spacecraft affect all ranges in the same way and are dealt with by the outer calibration. The outer calibration also transforms the measurements into the FSR system by aligning the OS x-axis to the inertial spin axis.

The input calibration parameters are:

$\mathcal{M}_{\mathrm{rot}}$ converts from the OS to the FSR system (spin axis alignment). It is determined by two Euler rotation angles: α_y around the y-axis and α_z around the z-axis.

$$\mathcal{M}_{\mathrm{rot}} = \begin{pmatrix} \cos\alpha_z & \sin\alpha_z & 0 \\ -\sin\alpha_z & \cos\alpha_z & 0 \\ 0 & 0 & 1 \end{pmatrix} \begin{pmatrix} \cos\alpha_y & 0 & \sin\alpha_y \\ 0 & 1 & 0 \\ -\sin\alpha_y & 0 & \cos\alpha_y \end{pmatrix} \tag{11}$$

$\mathcal{M}_{\mathrm{sc}}$ was introduced to correct for any residual nonorthogonality still present after the inner range-specific calibration. However, it was found not to be necessary, therefore $\mathcal{M}_{\mathrm{sc}}$ remained set to the identity matrix throughout the mission for all spacecraft and will be ignored from now on.

$\mathcal{M}_{\mathrm{cal}}^{(r)}$ is the range-specific calibration matrix Eq.(8) converting from the FS to the OS system and applying the gain correction. From the definition of the OS and FS systems results that the angles θ_x and φ_y are equal to zero. Therefore the range-specific calibration matrix is:

$$\mathcal{M}_{\mathrm{cal}}^{(r)} = \begin{pmatrix} 1/G_x & 0 & 0 \\ -\theta_y & 1/G_y & 0 \\ -\theta_z & \Delta\varphi_{yz} & 1/(G_y - \Delta G_{yz}) \end{pmatrix} . \tag{12}$$

Any deviation of the x-axis direction from the inertial spin axis is corrected by the $\mathcal{M}_{\mathrm{rot}}$ matrix. In this way, the orthogonalization is fully separated from the spin axis alignment.

$\mathbf{O}^{(r)}$ is the range-specific offset in the FS system.

$\mathbf{O}^{\mathrm{sc}}$ is the spacecraft generated offset in the OS system.

The calibration parameters have been accurately determined at the TU-Braunschweig Magnetsrode facility, prior to the lunch. However, various factors such as temperature

changes, mass redistribution due to fuel consumption, and ageing of instrument components lead to changes of the parameters. It is therefore necessary to periodically check and adjust in-flight these calibration parameters.

The calibration parameters can be divided into three categories according to the calibration method used to determine them:

1. Parameters which can be determined through Fourier analysis of the first and second harmonic of the spin tone ω:

   ω: α_y, α_z, $\theta_y^{(r)}$, $\theta_z^{(r)}$, $O_y^{(r)}$, $O_z^{(r)}$, O_y^{sc}, O_z^{sc}

   2ω: $\Delta\varphi_{yz}^{(r)}$, $\Delta G_{yz}^{(r)}$

2. Parameters which can be determined through solar wind analysis:

   $O_x^{(r)}$, O_x^{sc}

3. Parameters which can be determined through comparison with geomagnetic models if close enough to Earth.

   $G_x^{(r)}$, $G_y^{(r)}$

In the next subsections we outline the methods used to determine the Cluster FGM calibration parameters in the first two categories.

2.3.1 Power spectrum analysis

As noted above, deviations of the calibration parameters in the first category from their correct values lead to coherent signals at the first and second harmonic of the spin frequency. More precisely, a spin-tone signal results from errors in the elevation angles θ_y and θ_z, or in the spin plane offsets O_y and O_z. Errors in the spin plane gain mismatch ΔG_{yz} and in the spin plane nonorthogonality $\Delta\varphi_{yz}$ result in a signal at the double spin frequency.

These effects do not affect all components of the calibrated magnetic field in the same way, allowing for a more precise decoupling of the calibration parameters. A look at the Eq.(12) shows that errors in the calibration matrix $\mathcal{M}$ cannot lead to coherent spin related signals in the calibrated spin aligned B_x component. They can only affect the spin plane component $B_{yz} = \sqrt{B_y^2 + B_z^2}$. When the first harmonic of the spin frequency is observed in the spin plane component, an ambiguity still arises as of which calibration parameter is responsible for it. Both the spin plane elevation angles θ_y, θ_z and the spin plane offsets O_y, O_z could cause it. However, the effect is dependent on the magnetic field magnitude. Offsets are adjusted for low field intervals, orthogonality is adjusted for high field intervals. A spin tone signal in the spin aligned component can only originate from errors in the spin alignment matrix $\mathcal{M}_{\mathrm{rot}}$.

In summary, the calibration parameters in the first category are determined as follows:

- spin axis alignment α_y, α_z:
  minimize spin tone in the spin axis component B_x

- spin plane angles θ_y, θ_z:
  minimize spin tone in the spin plane component B_{yz} at high fields
- spin plane offsets O_y, O_z:
  minimize spin tone in the spin plane component B_{yz} at low fields
- spin plane nonorthogonality and spin plane gains mismatch $\Delta\varphi_{yz}$, ΔG_{yz}:
  minimize the second harmonic in the spin plane component B_{yz}

2.3.2 Solar wind analysis

The spin axis offset O_x can be determined from the incompressibility properties of the Alfvén waves (Belcher, 1973; Hedgecock, 1975; Leinweber et al., 2008). Because of their orbits, the Cluster spacecraft are immersed into the solar wind only during the "dayside season" lasting roughly from November to June each year. This precludes the determination of the spin axis offsets on a daily basis. To obtain an accurate offset estimation, the spacecraft should spend intervals of at least one day in the unperturbed solar wind (foreshock excluded). This only occurs towards the middle of the dayside season. Therefore an accurate calibration of the spin axis offsets is not possible on a daily basis neither during the entire dayside season. As a compromise, the spin plane offsets were determined once per year based on several hours intervals of measurements in the solar wind for all instrument ranges. For this purpose the instrument was set via ground commands into a special calibration mode which switches through all ranges at low fields. The obtained data was analysed and the offset minimizing the correlation between changes in the field magnitude and changes in the inclination of the field (Hedgecock, 1975) was selected. The determined spin axis offsets were considered valid until the following year solar wind calibration.

As more years of data were collected, it become possible to make a better estimation of the spin axis spacecraft offset O_x^{sc} using all available measurements in the solar wind. The idea is to determine an offset for each dayside season using all the available data and to calculate the daily spin axis offsets through an interpolation of the estimated yearly offsets.

For the selection of the solar wind intervals (SWI) we use the Geospace Region and Magnetospheric Boundary (GRMB) dataset (Grison et al., 2025). For each SWI (with length spanning roughly from 30 min to 30 h) we calculate a set of spin axis offsets using a 6 min widow slid with a 10 s step. For each window we apply the Davis-Smith method (Leinweber et al., 2008) and minimize the variation of the calibrated magnetic field magnitude while keeping the spin plane offsets constant at their already calibrated values.

The offset associated with each SWI is obtained through a Kernel Density Estimation (KDE, Scott, 2015) of the resulting set. Since during the dayside season there are typically multiple SWIs in one day, the daily offset is computed as a weighted average of the SWIs offsets in that day. For the weighting, the standard deviation of each set and the SWI length are used.

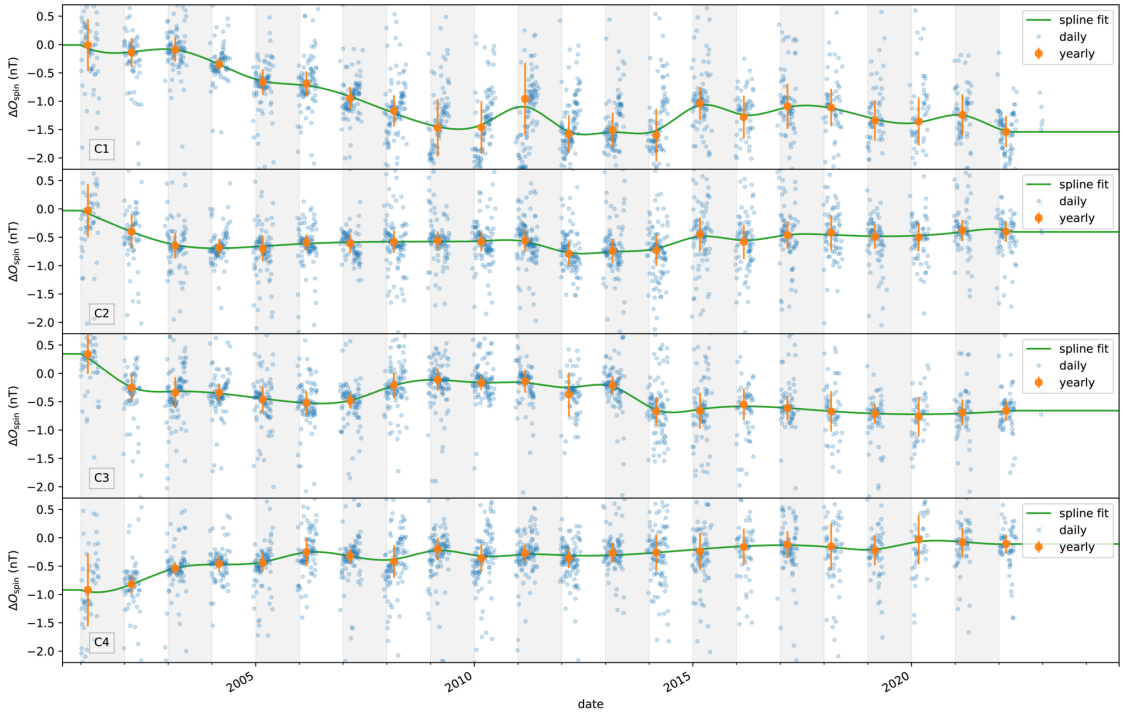

Figure 1: The spin axis spacecraft offsets O_x^{sc} adjustments from the beginning of mission values. The blue dots are the dayside season daily offsets resulted from the Davis-Smith method. The orange dots are the yearly offsets estimated from the maximum KDE of the daily offsets in the respective dayside season. The green line shows the final adjustments to the spin axis offsets.

Since no selection of intervals which are likely to contain Alfvén waves among the SWIs in the GRMB dataset is done, the daily offsets show a significant spread around the real offset. Therefore we use again a kernel density estimation of the daily offsets for each dayside season and we assign the result to the approximate middle of each season, 1st of March. These are the new yearly spin axis offsets.

To arrive at the final daily spin axis offsets we fit a cubic spline function to the yearly offsets. The spin axis offsets relative to their values at the beginning of the mission are shown in Figure 1 for all four Cluster spacecraft. The blue dots are the (dayside season) daily offsets. The orange dots are the yearly offsets, with error bars showing the standard deviation of the daily offsets for the respective season. The final daily offsets are depicted with the green line.

3 Cluster FGM daily calibration procedure

Much of the Cluster FGM calibration and data processing software developed organically inheriting code used for magnetometers onboard other missions such as the FGM onboard

the Equator-S spacecraft (Fornaçon et al., 1999; Haerendel, 2000). As a consequence, it incudes code written in C, Fortran, IDL, Perl, and Python. The software used to extract the raw data from the telemetry frames, to apply the calibration and to transform the calibrated magnetic field into various coordinate systems is written in C and Fortran. The software used to determine the calibration parameters based on Fourier analysis is written in IDL. Determination of the spin-axis offset in the solar wind is done using software written in Python. Automatization of the daily calibration of the spacecraft offset is done using Perl scripts.

3.1 Application of the calibration to the data

The raw data processing software is composed of modules which can be chained together to form a data processing pipeline. Various pipelines are used to produce the input data for calibration and the final calibrated data. All modules are described in the FGMDP.

The `fgmcal` module applies the calibration to the measured data. When applying the calibration it is no longer necessary to keep the parameters decoupled. Therefore the calibration equation Eq. (10) is condensed into a simpler form:

$$\mathbf{B}^{\mathrm{FSR}} = \mathcal{M}^{(r)}_{\mathrm{fgmcal}}\mathbf{B}^{\mathrm{FS}} - \mathbf{O}^{(r)}_{\mathrm{fgmcal}}\,. \tag{13}$$

where the range specific calibration matrix $\mathcal{M}^{(r)}_{\mathrm{fgmcal}}$ contains the scaling, the orthogonalization, and the alignment information. From Eq.(10) the first order of $\mathcal{M}^{(r)}_{\mathrm{fgmcal}}$ is:

$$\mathcal{M}^{(r)}_{\mathrm{fgmcal}} = \mathcal{M}_{\mathrm{rot}}\mathcal{M}^{(r)}_{\mathrm{cal}} = \begin{pmatrix} 1/G_x & \alpha_z & \alpha_y \\ -\alpha_z - \theta_y & 1/G_y & 0 \\ -\alpha_y - \theta_z & \Delta\varphi_{yz} & 1/(G_y - \Delta G_{yz}) \end{pmatrix}. \tag{14}$$

which is the calibration matrix in Eq.(8) with explicit rotations around the y and z axes. The range offset vector in the FSR frame is:

$$\mathbf{O}^{(r)}_{\mathrm{fgmcal}} = \mathcal{M}_{\mathrm{rot}}\mathbf{O}^{\mathrm{sc}} + \mathcal{M}_{\mathrm{rot}}\mathcal{M}^{(r)}_{\mathrm{cal}}\mathbf{O}^{(r)}\,. \tag{15}$$

The compact form of the daily calibration parameters are red from text files with the `fgmcal` extension.

3.2 Estimation of the calibration parameters

The routine of daily calibration follows the steps below:

1. Identify daily 5 min long intervals for spacecraft spin plane offsets calibration (O^{sc}_y and O^{sc}_z). These should be quiet, low field intervals with the instrument operating in range 2.

2. Estimate the spacecraft spin plane offsets for these intervals by minimizing the spin plane spin tone.

3. Produce daily spectrograms and time series plots around the range changes.

4. Visually inspect the daily spectrograms and the range change plots.

5. If anomalous spectral power is observed at the first or second harmonic of the spin frequency adjust the corresponding parameters.

6. If discontinuities are observed in the range changes plots adjust the corresponding parameters.

7. Archive the estimated calibration parameters in both `cfgnew` (extended calibration parameters used by Eq. (10)) and `fgmcal` (compact calibration parameters used by Eq. (13)) formats.

In addition, the spin axis spacecraft offsets O_x^{sc} must be estimated as described in Section 2.3.2.

4 Long-term trends and seasonal variations

The nearly quarter century long dataset of FGM calibration parameters for the four Cluster spacecraft reveals the exceptional stability of the instruments. The long-term variations were already investigated by Alconcel et al. (2014) based on the dataset available at the time, covering the first half of the mission. We extend the survey for the entire duration of the mission and can confirm most of the conclusions reached by Alconcel et al..

For each parameter we produced time series plots of the daily values over the entire mission duration together with the yearly averages and the yearly standard deviations. Only the plots of the spin axis alignment angles, spacecraft offset, range 4 offset and range 4 matrix for C1 are shown here. The rest of the parameters plots are included in the accompanying Supporting Information (SI).

Basic statistics were computed for each parameter and are presented in Tables 2 to 5. The columns *mission average* and *mean yearly standard deviation* are self-explanatory. Note that for some infrequently changed parameters – especially for ranges 6 and 7, but not only – statistical concepts such as the standard deviation loose their conventional meaning. The *decadal trend* column aims to quantify systematic overall drifts of the parameters from the beginning to the end of the mission, if present. A glance over the parameters plots shows that most parameters do not display an actual increasing or decreasing trend. For these parameters, the trend is set to zero in the tables. The remaining parameters tend to show a higher rate of change in the first years of the mission, followed by a lower rate or even quasi-constant values during the second half of the mission. This behaviour makes it problematic to describe the parameters trends. To keep the tables easy to digest, we decided to restrict the presented trend information to the slope of the linear trend. If the overall change is larger than three mean yearly standard deviations of the parameter, it is considered that a trend exists and the ten-year change is filled in the table. Otherwise the trend is set to zero in the table. To aid visualization of the tables, all zero values are greyed-out.

Below we discuss the long-term behaviour of a subset of calibration parameters.

4.1 Spin plane offsets

The spacecraft spin plane offsets O_y^{sc}, O_z^{sc}, as well as the range spin plane offsets $O_y^{(r)}$, $O_z^{(r)}$ are estimated through the minimization of the spin tone signal in the calibrated spin plane component B_{yz}.

The spacecraft spin plane offsets are illustrated in Figure 2 for C1 and in Figure S45, Figure S86, and Figure S127 of the accompanying SI for the other spacecraft. For C1 an overall trend is clearly observable in both components. From Table 2 we see that the trend of the O_y^{sc} component is about $1.7\,\mathrm{nT\,decade^{-1}}$ and the trend of the O_z^{sc} component is about $-0.8\,\mathrm{nT\,decade^{-1}}$. The spacecraft spin plane offsets of the other spacecraft do not show any relevant trend, except for the O_z^{sc} component of C4 which has a trend of $-0.3\,\mathrm{nT\,decade^{-1}}$. Where a trend is present, the rate of change tends to decrease towards the end of the mission.

All spin plane spacecraft offsets exhibit a clear seasonal variation which was linked by Alconcel et al. to the warming/cooling temperature cycles of the sensor temperature. The amplitude of the cycles changes significantly over the course of the mission. The largest peak to peak amplitude of the seasonal cycles, almost 2 nT, is reached for the C1 O_y^{sc} component in the last years of the mission. During the first years the amplitude of the seasonal cycles of both spin plane offset components is significantly lower. The pattern of the seasonal variations is different from spacecraft to spacecraft and from component to component.

The yearly standard deviation of the spin plane offsets reflects the amplitude of the seasonal variation. C1 has the largest mean yearly standard deviation of the spin plane spacecraft offsets, equal to 0.3 nT for O_y^{sc} and 0.2 nT for O_z^{sc}. For the other spacecraft this quantity is around 0.1 nT.

Since the spacecraft offsets are always determined using range 2 data, the range 2 offsets are directly tied to the spacecraft offsets and are kept constant during the mission. No trends of the spin plane offsets are observed in range 3 and their overall variation in this range is below 0.3 nT for all spacecraft. The mean yearly standard deviations for the range 3 offsets are insignificant for all four spacecraft (below 0.05 nT).

Reaching values of $2.7\,\mathrm{nT\,decade^{-1}}$ and $-1.4\,\mathrm{nT\,decade^{-1}}$ the spin plane offsets of range 4 of C1 display some of the strongest offset trends. Figure 3 shows a very clear long-term trend of all offset components. An overall change in $O_y^{(4)}$ of roughly 8 nT and in $O_z^{(4)}$ of roughly 3 nT takes place before 2012. After this date only seasonal cycles affect the offsets. Similar but much weaker variations can be observed for range 4 of C2 in Figure S47. No significant trends are observed for the spin plane offsets in range 4 of C3 and C4.

Even though range 5 commenced operating only in 2006, the range 5 spin plane offset of C1 behaves similarly to the range 4 spin plane offset, as it can be seen in Figure S7. No clear trends are observed for the range 5 spin plane offsets of the other spacecraft though.

While the variations of the range 6 and range 7 offsets are significant, no clear trend can be identified for these ranges.

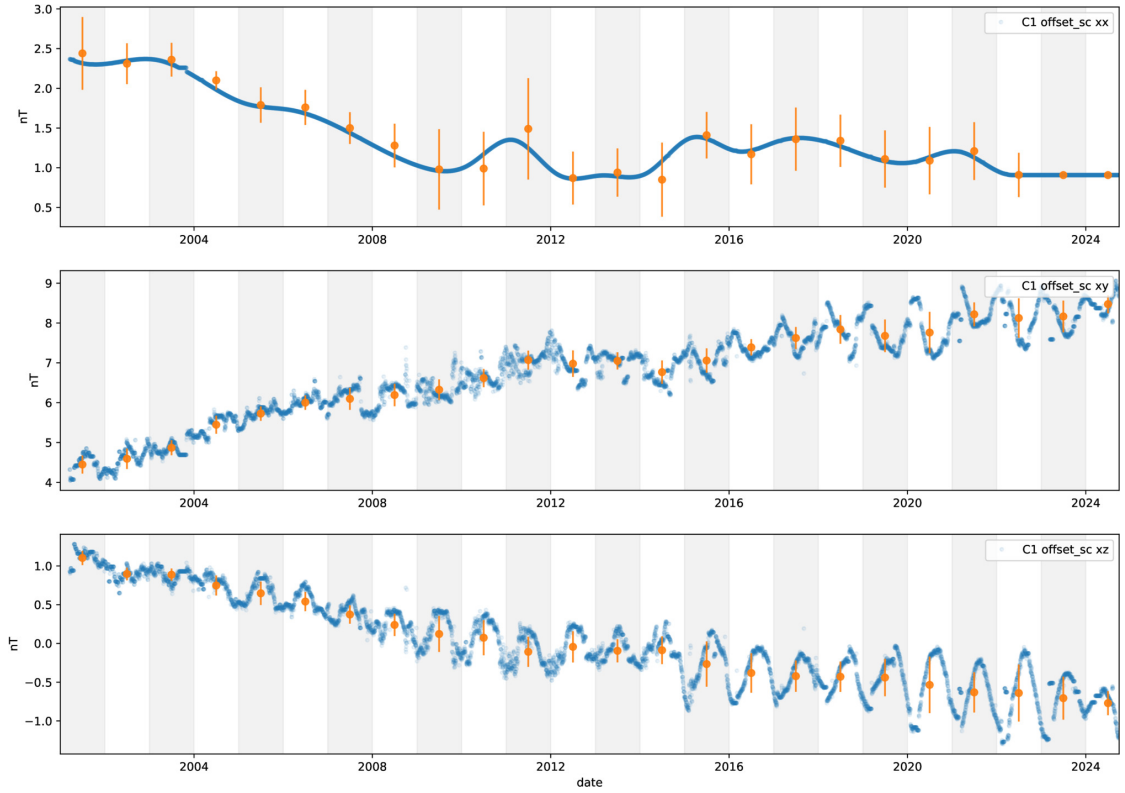

Figure 2: The spacecraft offsets for C1. The daily offsets are represented by the blue dots, the yearly averages are plotted with orange dots. The error-bars are the standard deviations for each year.

4.2 Spin axis offsets

The spacecraft spin axis offsets O_x^{sc} are estimated as described in Section 2.3.2. The estimation procedure obscures potential seasonal cycles likely similar to the spin plane component offsets variations. The overall trend however follows the trends observed in the spin plane components.

The spin axis offsets of the ranges are determined by requiring that no discontinuity of the measurements occurs when the instrument switches between the ranges. As in the case of the spin plane offsets, range 2 offsets are kept constant. The spin axis offsets of the higher ranges mirror the behaviour of the spin plane offsets. The range 4 offset of C1 presents the strongest trend among all ranges and all spacecraft reaching over $10\,\mathrm{nT\,decade^{-1}}$ with the bulk of the change occurring in the first half of the mission.

4.3 Spin axis alignment angles

Despite being placed at the tips of 5 m long booms, the alignment relative to the inertial spin axes of the sensor coils measuring the spin aligned magnetic field is better than 1°.

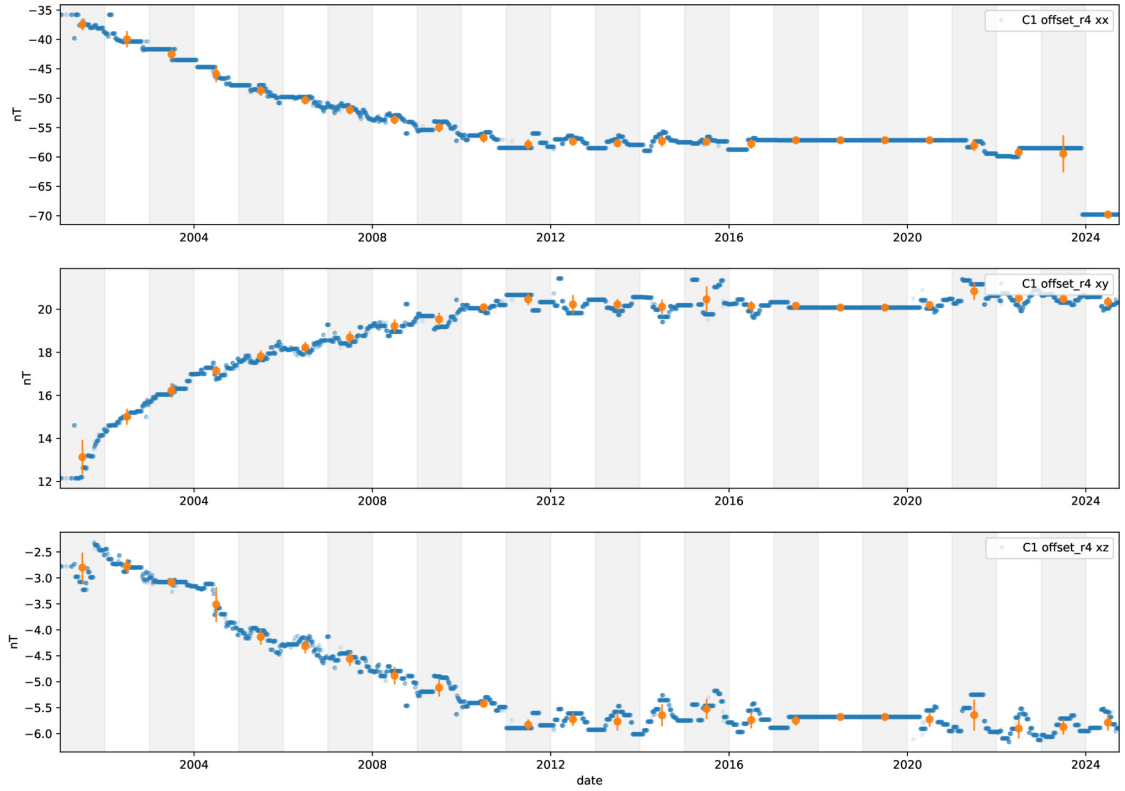

Figure 3: The range 4 offsets for C1. The daily offsets are represented by the blue dots, the yearly averages are plotted with orange dots. The error-bars are the standard deviations for each year.

The in-flight determination of the alignment angles is done by minimizing the spin tone signal in the spin axis component of the calibrated magnetic field. If the alignment is done using high field data this method delivers arcsecond order precision. The largest mean yearly standard deviations of the determined spin alignment angles are around $1'$ for C1. For the other spacecraft the mean yearly standard deviations are between $7''$ and $14''$. The long-term trends of the spin alignment angles are below $1'\,\mathrm{decade}^{-1}$ for all spacecraft.

4.4 Spin plane angles

Figure 5 illustrates the range 4 calibration matrix of C1. The subplots are arranged following the order of the matrix elements. The lower two elements of the first column of the range calibration matrices are linked to the deviations from orthogonality of the angles between y_{FS} and x_{FS}, and between z_{FS} and x_{FS} axes of the FGM sensor system, expressed in radians. These elements are determined through the minimization of the spin tone in the spin plane component of the calibrated magnetic field. To separate from the effects of errors in the spin plane offsets, the estimation of the spin plane angles is

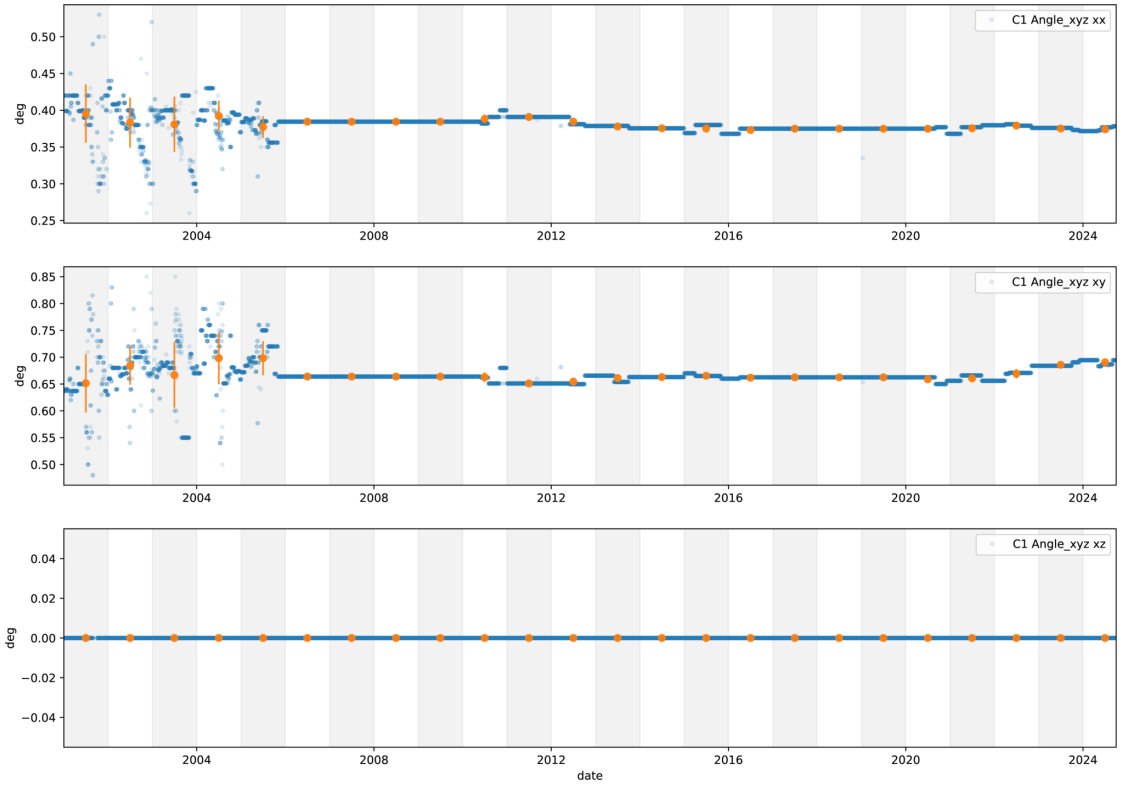

Figure 4: The spin axis alignment angles as rotation angles around the z, y, and x axes in this order for C1. The daily values are represented by the blue dots, the yearly averages are plotted with orange dots. The error-bars are the standard deviations for each year.

done using the highest fields measured by the range being calibrated. The variations of these angles over the course of the the mission are very low, as are also the observed trends. This applies for the other spacecraft and other ranges too. While the conditions set by us to identify trends are met for some spin plane angle of some of the spacecraft, because the changes of these elements are very small and infrequent, the existence of trends is sometimes not evident from the plots.

4.5 Spin plane nonorthogonality

The deviation from orthogonality of the angle between the y_{FS} and z_{FS} axes of the FGM sensor system affects the middle element of the last row of the calibration matrix $\mathcal{M}^{(r)}$. This element is determined together with its right neighbour by minimizing the spectral power of the second harmonic of the spin frequency. For C1 the long-term variation of the ranges 2 to 5 spin-plane nonorthogonality resembles the variation of the range offsets, with almost all the change concentrated in the first half of the mission. The other spacecraft exhibit similar behaviour in these ranges, albeit not always displaying

such a clear variation. Ranges 6 and 7 do not show any consistent trend for neither spacecraft.

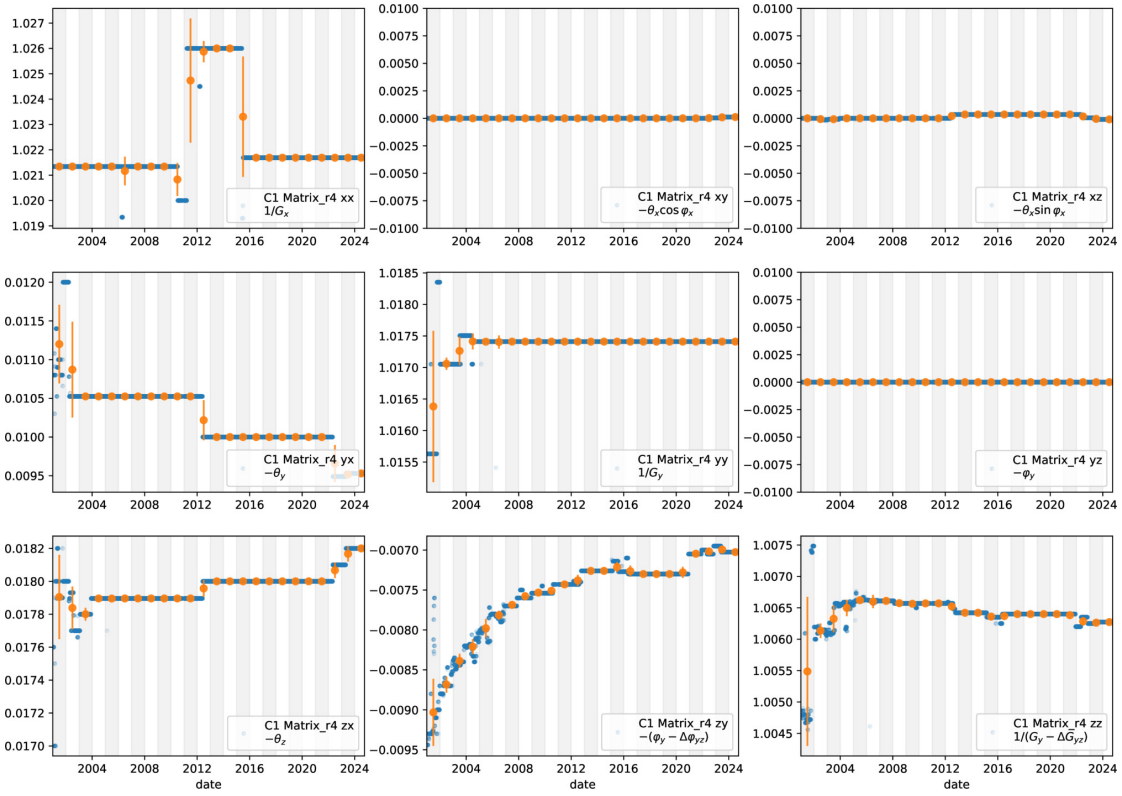

Figure 5: The range 4 calibration matrix for C1. The panel order follows the actual order of the matrix elements. The daily values are represented by the blue dots, the yearly averages are plotted with orange dots. The off-diagonal elements are expressed in radians. The diagonal elements are dimensionless. The error-bars are the standard deviations for each year.

4.6 Spin plane gain mismatch

The difference between spin plane gains, $\Delta G_{yz}^{(r)}$ affects the other matrix element which is determined through the minimization of the second harmonic, the last diagonal element. The long-term variations of $\Delta G_{yz}^{(r)}$ is are less ordered than the variations of the spin plane nonorthogonality with the exception of range 3 of C2 as seen in Figure S52. Both the mean yearly standard deviations and the overall change of the spin plane mismatch during the mission are not significant for any Cluster spacecraft.

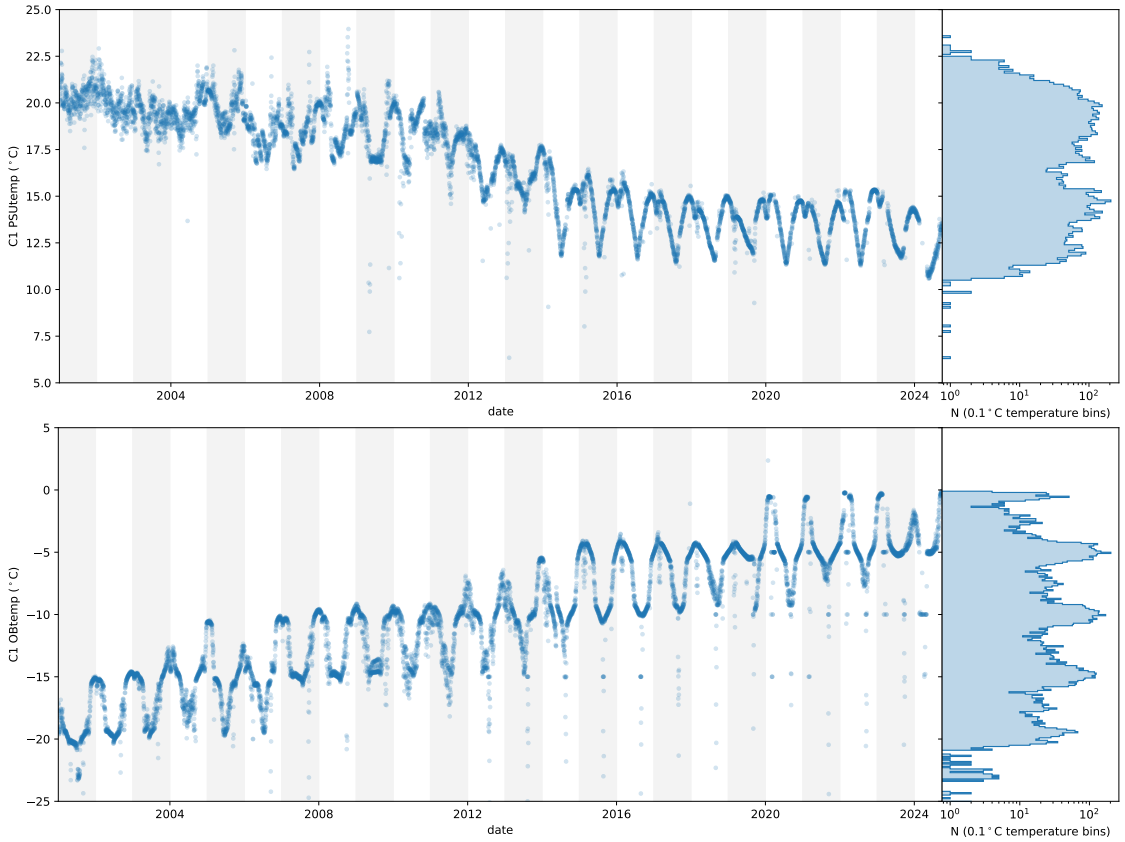

Figure 6: The daily averaged electronics box (top panel) and outboard sensor (bottom panel) temperatures for C1. The histograms on the right of the panels show the occurrence frequency the of registered daily temperatures in 0.1 °C bins.

4.7 The effect of the temperature on the calibration parameters

As noted by Alconcel et al. (2014) the variation of some calibration parameters is linked to the variation of the sensor and/or of the electronics box temperature. Both temperatures are recorded with a time resolution of about 5 s. The daily averages of these temperatures for Cluster 1 are presented in Figure 6. The left side of the panels show the time series of the temperatures, while the occurrence frequency the of registered daily averages in 0.1 °C bins is illustrated by the histograms on the right side of the panels. The seasonal variation, evident for both temperature sets is due to the yearly shift of the perigee from the dayside to the nightside. The sudden temperature drops seen in the figure are caused by eclipses.

The measurement resolution of the electronics box temperature is 0.1 °C, sufficient for fair representation of the roughly 15 °C interval containing most of the measurements. The situation is different for the outboard temperature measurements: The interval of roughly 20 °C containing most of the measurements is covered with a resolution of 5 °C. The effect of this low measurement resolution is clearly visible in the 5 °C separated

peaks of the histogram. The low measurements resolution limits the accuracy of the analysis of the effect of the sensor temperature on the calibration parameters.

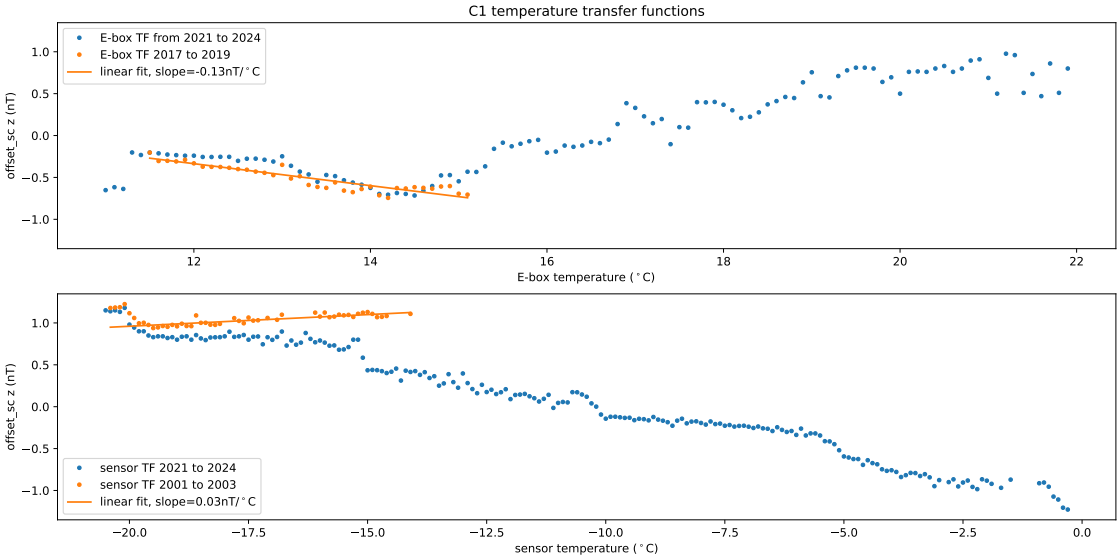

Figure 7: The sensor temperature effect on the z-component of the spacecraft offset for C1. The dots represent the average over 0.1 °C temperature bins of O_z^{sc}. The averages from the entire mission span are represented with blue colour, the averages from selected 3 years time intervals (2017.01.01 to 2019.12.31 for the E-box; 2001.01.01 to 2003.12.31 for the sensor) are represented with orange colour. The orange lines represent linear fits for the selected intervals.

Unlike the seasonal variations which are in phase for both temperatures, the long-term trend is opposite: the electronics box temperature follows a decreasing trend while the outboard sensor temperature follows an increasing trend. The electronics box temperature is linked to the overall spacecraft body temperature, the observed cooling reflecting changes in the spacecraft heating strategy over the course of the mission (Alconcel et al., 2014). The warming trend of the outboard sensor is probably due to a combination between changes in the orbital parameters and ageing of the thermal insulation of the sensor.

To investigate the relation between the sensors/electronics temperatures and the calibration parameters we divide the calibration parameters into groups corresponding to 0.1 °C bins of the daily averaged temperature and compute the parameter average for each bin. Plots of all parameters versus the sensor temperature and versus the electronics box temperature are given in the Supporting Information.

Changes in the sensor properties are due either to ageing or to temperature changes. The same is true for the electronics box. All these changes translate into changes of the calibration parameters. In the ideal case, the range-specific parameters appearing in Eq. (10) (i.e. $\mathcal{M}_{\mathrm{cal}}^{(r)}$ and $\mathbf{O}^{(r)}$) should be affected by the electronics box temperature, while the other parameters (i.e. $\mathcal{M}_{\mathrm{rot}}$ and $\mathbf{O}^{\mathrm{sc}}$) should be independent on the electronics

box temperature. However, as discussed in Section 4.1, the spacecraft offset and the alignment angles are in practice determined using measurements within a certain range, mixing in therefore effects from both the sensor and the electronics. Each calibration parameter have its own dependency on time and temperatures, many times non-linear. Since a detailed characterization of the temperature impact on all calibration parameters is beyond the scope of this work, we will limit our analysis to the z component of Cluster 1 spacecraft offset ${}^{\mathrm{C1}}O_z^{\mathrm{sc}}$.

All four types of effects contribute to the variation of the spacecraft offset (ageing of the sensor, ageing of the electronics, sensor temperature, and electronics box temperature). The trend of the offset is caused by all four effects. The seasonal cycles though, are independent of the ageing offering a way to decouple ageing from temperature effects.

We note that in the first 4 years of the mission the electronics box temperatures for all spacecraft show very low seasonal variation, probably due to a more active use of heating to compensate the variation in the spacecraft temperature. In contrast, during the same period, the outboard sensors temperatures show a strong seasonal variation. Yet, no component of ${}^{\mathrm{C1}}O_z^{\mathrm{sc}}$ reflects the seasonal cycles of the sensor temperature during this time. Therefore, at least during the first 4 years and inside the temperature ranges spanned during this interval, the spacecraft offset is very weakly coupled to the sensor temperature. To estimate an upper limit of the coupling coefficient (assuming linear dependence of the offset on sensor temperature inside the small 5 °C temperature range) we restrict the time interval to the years 2001, 2002 and 2003 and de-trend the offset to eliminate the ageing effect before computing the temperature bins averages. The result is shown in the bottom panel of Figure 7. The blue dots in the figure are the (not de-trended offset) averages in each sensor temperature bin for the entire mission. The orange dots are the (de-trended offset) averages for the years 2001, 2002 and 2003. The orange line is the linear fit for this restricted time interval. The fit indicates an upper limit of $0.03\,\mathrm{nT\,°C^{-1}}$ for the coupling coefficient between ${}^{\mathrm{C1}}O_z^{\mathrm{sc}}$ and the sensor temperature.

Turning out attention to the electronics box temperature we observe that in the last years of the mission it undergoes significant seasonal cycles but its long-term trend is negligible. The large amplitude seasonal cycles of ${}^{\mathrm{C1}}O_z^{\mathrm{sc}}$ during this time suggest a strong coupling with the electronics box temperature (assuming a weak coupling with the sensor temperature, similar with the one derived above). We select the years 2017, 2018 and 2019 and repeat the analysis above using the electronics box temperature. The result is plotted in the top panel of Figure 7. Indeed, the resulting coupling coefficient between ${}^{\mathrm{C1}}O_z^{\mathrm{sc}}$ and the electronics box temperature is $-0.13\,\mathrm{nT\,°C^{-1}}$, four times larger than the coupling with the sensor temperature.

We are now in position to check how well the assumption of linear dependence of ${}^{\mathrm{C1}}O_z^{\mathrm{sc}}$ on time, sensor temperature, and electronics box temperature describes the reality. We consider the offset variation to be the sum of individual effects:

$$ {}^{\mathrm{C1}}O_z^{\mathrm{sc}} = O_0 + C_{\mathrm{ageing}}t + C_{\text{e-box}}T_{\text{e-box}} + C_{\mathrm{sensor}}T_{\mathrm{sensor}}, \tag{16} $$

where O_0 is the initial offset in the absence of temperature effects, C_{ageing} is the rate of change in time due to ageing of both sensor and electronics, t is the time, $C_{\text{e-box}}$ is the

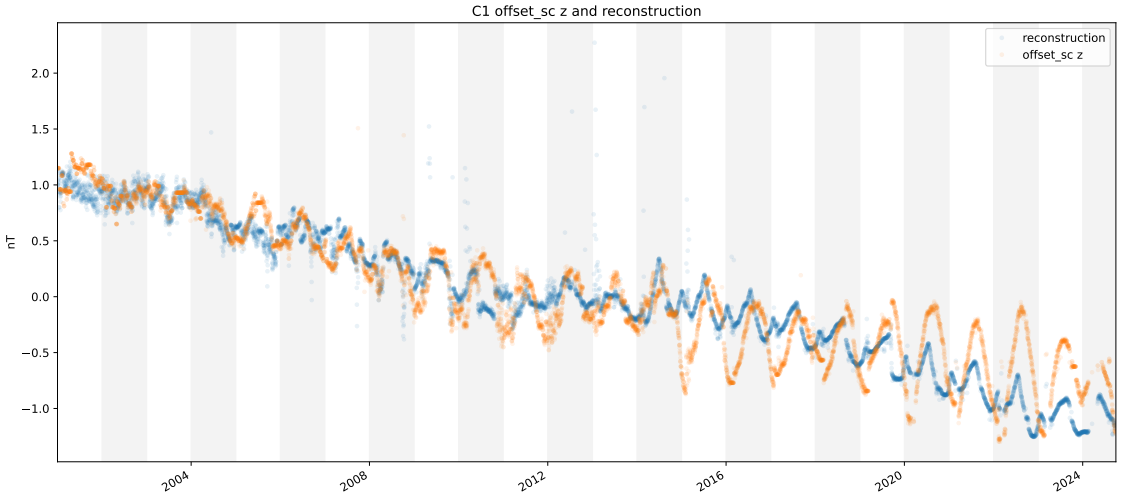

Figure 8: The Cluster 1 z-component of the spacecraft offset (orange) and its reconstruction from Eq.(17) (blue).

coupling coefficient to the electronics box temperature $T_{\text{e-box}}$, and C_{sensor} is the coupling coefficient to the sensor temperature T_{sensor}. The only variables missing from Eq.(16) are the initial offset O_0 and the rate of change in time C_{ageing}. They can be obtained through a linear fit of the difference between the measured offset ${}^{\text{C1}}O_z^{\text{sc}}$ and the temperature terms $(C_{\text{e-box}}T_{\text{e-box}} + C_{\text{sensor}}T_{\text{sensor}})$. The result is O_0=4.24 nT and C_{ageing}=−1.5 nT decade^{-1}. Since the total rate of change of ${}^{\text{C1}}O_z^{\text{sc}}$ is −0.8 nT decade^{-1} (see Table 2) it results that in this case the ageing trend opposes the trend due the temperature trend. Eq.(16) can be written as:

$$ {}^{\text{C1}}O_z^{\text{sc}} = 4.24 - 1.5t - 0.13T_{\text{e-box}} + 0.03T_{\text{sensor}}. \tag{17} $$

We can now reconstruct the offset based on Eq.(16). Figure 8 shows the original offset ${}^{\text{C1}}O_z^{\text{sc}}$ using the orange colour and the reconstructed offset using blue colour. The reconstructed offset reproduces well the original offset until 2015. After this time the reconstructed offset reflects second harmonics in the yearly cycles present in the electronics box temperature but absent in ${}^{\text{C1}}O_z^{\text{sc}}$.

4.8 Comparison with previous analysis

Our analysis of the calibration parameters generally agrees with the analysis carried out by Alconcel et al. (2014). It is important to note though, that the calibration strategy adopted by Alconcel et al. is slightly different from the procedure presented in Section 2.3. Instead of determining the calibration parameters in Eq.(10), Alconcel et al. determined the elements of the compact calibration matrix Eq.(14) and the offsets Eq.(15).

This approach turns all the calibration parameters in range-specific parameters, mixing in the spacecraft influence with electronics related effects. Moreover, now a change in the spin-axis angles implies a change in the orthogonality. With this in mind, there

is a good agreement between the statistical analysis results presented in this work and those of Alconcel et al. (2014).

5 Calibration impact on the accuracy of the calibrated magnetic field

The errors of the calibrated magnetic field due to deviations of the calibration parameters from their correct values can be computed based on the calibration equation Eq.(10). The individual effect of a deviation δ of a single calibration parameter p from its correct value p_0 can be estimated as

$$\epsilon_p(\delta) = \frac{1}{2}\left(|\mathbf{B}_{\rm cal}(p_0) - \mathbf{B}_{\rm cal}(p_0 - \delta)| + |\mathbf{B}_{\rm cal}(p_0) - \mathbf{B}_{\rm cal}(p_0 + \delta)|\right), \tag{18}$$

where $\mathbf{B}_{\rm cal}(p)$ is the result of the magnetic field calibration using the correct values for all parameters except for parameter p. The upper limit of the calibration error in the magnetic field is obtained by summing the individual effects for all calibration parameters.

We use the mission average of the calibration parameters as etalon, and the mean yearly standard deviations to represent the deviations δ. The mean yearly standard deviations depart from the real deviations of the calibration parameters as used in the daily calibration in two circumstances:

(1) For parameters going through seasonal cycles the yearly standard deviation overestimates the real deviations of the calibration parameters from their correct values. This leads to a gross overestimation of the spin plane error due to the spacecraft offsets.

(2) As noted at the beginning of this section, the standard deviations computed for infrequently changed parameters is not an accurate representation of their statistical behaviour. As a result, the calibration errors estimated for the ranges 6 and 7 are not reliable.

The magnetic field calibration errors computed using Eq.(18) are shown for C1 in Figure 9. The errors are displayed split on six stacked groups of parameters: $\mathbf{O}^{\rm sc}$, $\mathbf{O}^{(\rm r)}$, (α_y, α_z), (θ_y, θ_z), $\Delta\varphi_{yz}$, and ΔG_{yz}. The spin axis component errors are shown in the top panel, the spin plane component errors are shown in the bottom panel. Due to the issues mentioned above, the derived errors represent a reasonable error estimation only for ranges 2 to 5. One should also keep in mind the overestimation of the spin plane error due to the spacecraft offset. Note that these errors are linked to the daily calibration and do not reflect the accuracy of the data archived at the Cluster Science Archive (ESA, 2013) which was calibrated based on a different set of calibration parameters.

6 Summary and conclusions

This work reviews the theoretical basis of the algorithms used to calibrate the Cluster FGM instruments and presents their specific implementation. In addition, the behaviour

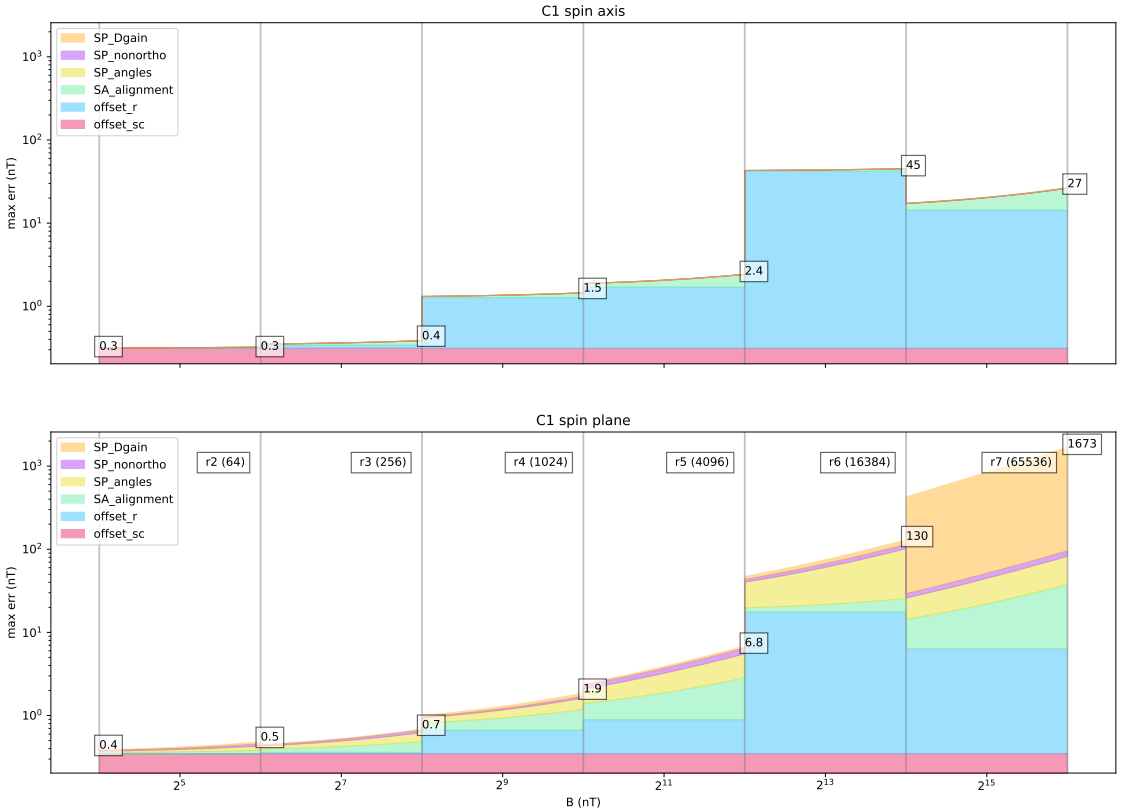

Figure 9: The maximum expected calibration errors for C1. The effects due to each calibration parameter are stacked vertically. SP stands for spin plane, SA stands for spin axis. The boxed numbers are the maximum errors for each range. Ranges 6 and 7 are included only for reference, the estimated errors for these ranges are not reliable.

of the calibration parameters determined over the course of the 24 years long mission is analysed.

The statistical analysis of the long-term variations of the calibration parameters of the Cluster FGM instruments demonstrate a remarkable stability of both the instruments and of the spacecraft over a very long period of space flight. The stability of some calibration parameters improves in time, with much reduced variations after the first 12 years. This might be related to the reduced long-term trend of the electronics boxes temperature in the second half of the mission.

Systematic long-term trends were observed for the spacecraft offsets, most probably stemming from magnetic fields produced by ageing of the sensors and of the associated electronics. Systematic trends were also observed for range specific offsets, most probably related to the electronics response to temperature changes. The largest trend was about $10\,\mathrm{nT\,decade^{-1}}$ observed for the C1 range 4 spin axis offset. The largest spacecraft offset trend was about $2\,\mathrm{nT\,decade^{-1}}$ observed for the O_y^{sc} component for the same spacecraft.

Clear long-term trends were also observed for the spin plane nonorthogonality angles for all spacecraft. The largest trend for this parameter was also observed for C1. In range 3 the observed trend was about $8'\,\mathrm{decade}^{-1}$.

The long-term trends of the other parameters are negligible.

Seasonal cycles of the spin plane components of the spacecraft offsets were observed for all spacecraft. The largest peak to peak seasonal variation was about 2 nT, observed for C1. Seasonal variations of range offsets were observed only for ranges 4 and 5 of C1 for all offset components. The amplitudes of the cycles were below 1 nT.

When present, both the long-term trends and the seasonal cycles are (mostly nonlinearly) coupled to the sensors and electronics boxes temperatures. The spacecraft offset rate of change with the temperature is below $0.3\,\mathrm{nT}\,^{\circ}\mathrm{C}^{-1}$. We annalized in detail the effect of the sensor temperature and of the electronics box temperature on the z-component of Cluster 1. Assuming linear relations we obtained a rate of change due to combined ageing of sensor and electronics equal to $-1.5\,\mathrm{nT\,decade}^{-1}$, a coupling coefficient to the electronics box temperature equal to $-0.13\,\mathrm{nT}\,^{\circ}\mathrm{C}^{-1}$, and a coupling coefficient to the sensor temperature equal to $0.03\,\mathrm{nT}\,^{\circ}\mathrm{C}^{-1}$.

Acknowledgments

This work is dedicated to Edita Georgescu (1956-2012). This work was financially supported by the Deutsches Zentrum für Luft- und Raumfahrt under contract 50 OC 2401. We thank Laakso et al. (2010) for their efforts in providing Cluster mission data and user guides through the Cluster Science Archive (CSA), and we acknowledge in particular the work of the whole FGM team.

Table 2: Cluster 1 FGM calibration parameters statistics over the entire mission lifetime. Offsets are expressed in nT, angles in degrees, matrix elements are adimensional factors.

parameter	mission average	mean yearly standard deviation	decadal trend
offset_r2	[−5.0 0.9 −0.1]	[0.0 0.0 0.0]	[0.0 0.0 0.0]
offset_r3	[−5.1 0.9 −0.1]	[0.0 0.0 0.0]	[0.0 0.0 0.0]
offset_r4	[−54.3 19.2 −5.1]	[0.9 0.3 0.2]	[−10.9 2.7 −1.4]
offset_r5	[−52.1 18.9 −4.8]	[1.4 0.5 0.2]	[−6.2 1.1 −0.8]
offset_r6	[−440.4 185.0 −30.0]	[41.2 16.9 3.1]	[0.0 0.0 0.0]
offset_r7	[−688.5 305.1 −31.1]	[14.0 6.0 0.9]	[0.0 0.0 0.0]
offset_sc	[1.4 6.8 0.0]	[0.3 0.3 0.2]	[−0.7 1.7 −0.8]
Angle_xyz	[0.3807 0.6676 0.0000]	[0.0102 0.0168 0.0000]	[0.0000 0.0000 0.0000]
Matrix_r2	[1.0523 0.0000 0.0003 ; 0.0106 1.0522 0.0000 ; 0.0179 −0.0035 1.0350]	[0.0000 0.0000 0.0004 ; 0.0006 0.0000 0.0000 ; 0.0002 0.0004 0.0004]	[0.0000 0.0000 0.0000 ; 0.0000 0.0000 0.0000 ; 0.0000 0.0020 0.0000]
Matrix_r3	[1.0343 0.0000 0.0002 ; 0.0100 1.0337 0.0000 ; 0.0181 −0.0030 1.0178]	[0.0009 0.0000 0.0002 ; 0.0004 0.0000 0.0000 ; 0.0001 0.0002 0.0001]	[0.0000 0.0000 0.0000 ; −0.0009 0.0000 0.0000 ; 0.0003 0.0024 −0.0003]
Matrix_r4	[1.0223 0.0000 0.0001 ; 0.0102 1.0173 0.0000 ; 0.0180 −0.0076 1.0064]	[0.0013 0.0000 0.0001 ; 0.0003 0.0003 0.0000 ; 0.0001 0.0001 0.0002]	[0.0000 0.0000 0.0000 ; −0.0006 0.0000 0.0000 ; 0.0001 0.0008 0.0000]
Matrix_r5	[1.0062 0.0000 0.0002 ; 0.0105 0.9995 0.0000 ; 0.0175 −0.0081 0.9896]	[0.0016 0.0000 0.0002 ; 0.0003 0.0004 0.0000 ; 0.0003 0.0002 0.0001]	[0.0000 0.0000 0.0000 ; −0.0012 0.0000 0.0000 ; 0.0009 0.0003 0.0000]
Matrix_r6	[1.0184 0.0000 0.0000 ; 0.0063 1.0118 0.0000 ; 0.0113 −0.0052 1.0064]	[0.0055 0.0000 0.0001 ; 0.0019 0.0028 0.0000 ; 0.0026 0.0008 0.0009]	[0.0000 0.0000 0.0000 ; 0.0000 0.0000 0.0000 ; 0.0000 0.0000 0.0000]
Matrix_r7	[1.0010 0.0000 0.0000 ; 0.0099 0.9994 0.0000 ; 0.0179 −0.0071 0.9897]	[0.0252 0.0000 0.0000 ; 0.0002 0.0242 0.0000 ; 0.0004 0.0002 0.0241]	[0.0000 0.0000 0.0000 ; 0.0000 0.0000 0.0000 ; 0.0000 0.0000 0.0000]

Table 3: Cluster 2 FGM calibration parameters statistics over the entire mission lifetime. Offsets are expressed in nT, angles in degrees, matrix elements are adimensional factors.

parameter	mission average	mean yearly standard deviation	decadal trend
offset_r2	[1.2 0.3 −0.5]	[0.0 0.0 0.0]	[0.0 0.0 0.0]
offset_r3	[1.3 0.3 −0.5]	[0.0 0.0 0.0]	[0.0 0.0 0.0]
offset_r4	[4.0 0.3 −0.2]	[0.1 0.1 0.0]	[0.0 −0.2 −0.3]
offset_r5	[5.1 1.2 0.7]	[0.2 0.1 0.1]	[0.0 0.0 0.0]
offset_r6	[22.9 −5.5 −1.5]	[3.3 1.4 1.0]	[0.0 0.0 −2.3]
offset_r7	[54.3 −0.8 6.8]	[0.2 0.5 0.6]	[0.0 0.0 0.0]
offset_sc	[−1.3 −2.9 −0.7]	[0.2 0.2 0.1]	[0.0 0.0 0.0]
Angle_xyz	[−0.1627 0.3328 0.0000]	[0.0020 0.0025 0.0000]	[−0.0098 0.0065 0.0000]
Matrix_r2	[1.0422 0.0000 0.0000 ; −0.0123 1.0491 0.0000 ; 0.0047 −0.0115 1.0555]	[0.0000 0.0000 0.0000 ; 0.0001 0.0000 0.0000 ; 0.0002 0.0001 0.0001]	[0.0000 0.0000 0.0000 ; 0.0000 0.0000 0.0000 ; 0.0000 0.0000 0.0002]
Matrix_r3	[1.0256 0.0000 0.0000 ; −0.0125 1.0316 0.0000 ; 0.0044 −0.0113 1.0389]	[0.0000 0.0000 0.0000 ; 0.0001 0.0000 0.0000 ; 0.0003 0.0001 0.0001]	[0.0000 0.0000 0.0000 ; −0.0002 0.0000 0.0000 ; 0.0000 0.0002 0.0002]
Matrix_r4	[1.0136 0.0000 0.0000 ; −0.0125 1.0196 0.0000 ; 0.0045 −0.0113 1.0154]	[0.0000 0.0000 0.0000 ; 0.0002 0.0003 0.0000 ; 0.0001 0.0001 0.0000]	[0.0000 0.0000 0.0000 ; 0.0000 0.0000 0.0000 ; −0.0003 0.0001 0.0001]
Matrix_r5	[0.9962 0.0000 0.0000 ; −0.0121 1.0025 0.0000 ; 0.0050 −0.0106 0.9994]	[0.0009 0.0000 0.0000 ; 0.0001 0.0006 0.0000 ; 0.0003 0.0002 0.0001]	[0.0000 0.0000 0.0000 ; −0.0004 0.0000 0.0000 ; −0.0009 0.0000 0.0000]
Matrix_r6	[1.0100 0.0000 0.0000 ; −0.0073 1.0138 0.0000 ; 0.0031 −0.0071 1.0106]	[0.0021 0.0000 0.0001 ; 0.0021 0.0028 0.0000 ; 0.0007 0.0008 0.0013]	[0.0000 0.0000 0.0000 ; 0.0000 0.0000 0.0000 ; 0.0000 0.0000 0.0000]
Matrix_r7	[0.9865 0.0000 −0.0002 ; −0.0117 0.9919 0.0000 ; 0.0050 −0.0111 0.9879]	[0.0001 0.0000 0.0000 ; 0.0000 0.0001 0.0000 ; 0.0000 0.0000 0.0000]	[0.0000 0.0000 0.0000 ; 0.0000 0.0000 0.0000 ; 0.0000 0.0000 0.0000]

Table 4: Cluster 3 FGM calibration parameters statistics over the entire mission lifetime. Offsets are expressed in nT, angles in degrees, matrix elements are adimensional factors.

parameter	mission average	mean yearly standard deviation	decadal trend
offset_r2	[0.2 −2.0 −0.9]	[0.0 0.0 0.0]	[0.0 0.0 0.0]
offset_r3	[0.2 −2.0 −0.9]	[0.0 0.0 0.0]	[0.0 0.0 0.0]
offset_r4	[6.5 4.7 4.1]	[0.1 0.1 0.1]	[0.0 0.0 0.0]
offset_r5	[7.4 5.4 4.4]	[0.2 0.1 0.1]	[0.0 0.0 0.0]
offset_r6	[75.1 77.3 63.7]	[27.4 23.8 20.0]	[0.0 0.0 0.0]
offset_r7	[120.4 121.7 95.5]	[2.5 2.6 2.3]	[0.0 0.0 0.0]
offset_sc	[−2.7 −3.1 −1.6]	[0.2 0.1 0.1]	[−0.3 0.0 0.0]
Angle_xyz	[0.8034 −0.1749 0.0000]	[0.0015 0.0023 0.0000]	[−0.0062 0.0057 0.0000]
Matrix_r2	[1.0422 0.0000 0.0000 ; 0.0057 1.0355 0.0000 ; −0.0068 −0.0135 1.0553]	[0.0000 0.0000 0.0000 ; 0.0002 0.0000 0.0000 ; 0.0001 0.0001 0.0001]	[0.0000 0.0000 0.0000 ; 0.0000 0.0000 0.0000 ; 0.0000 0.0000 0.0000]
Matrix_r3	[1.0238 0.0000 0.0000 ; 0.0057 1.0198 0.0000 ; −0.0068 −0.0134 1.0372]	[0.0000 0.0000 0.0000 ; 0.0002 0.0000 0.0000 ; 0.0002 0.0001 0.0001]	[0.0000 0.0000 0.0000 ; 0.0000 0.0000 0.0000 ; 0.0000 −0.0002 0.0000]
Matrix_r4	[1.0041 0.0000 0.0000 ; 0.0059 1.0061 0.0000 ; −0.0066 −0.0121 1.0194]	[0.0002 0.0000 0.0000 ; 0.0001 0.0002 0.0000 ; 0.0001 0.0001 0.0001]	[0.0000 0.0000 0.0000 ; 0.0000 0.0000 0.0000 ; 0.0000 0.0001 0.0000]
Matrix_r5	[0.9890 0.0000 0.0000 ; 0.0053 0.9912 0.0000 ; −0.0075 −0.0121 1.0024]	[0.0008 0.0000 0.0000 ; 0.0005 0.0002 0.0000 ; 0.0008 0.0001 0.0001]	[0.0000 0.0000 0.0000 ; 0.0000 0.0000 0.0000 ; 0.0000 0.0000 −0.0002]
Matrix_r6	[1.0032 0.0000 0.0000 ; 0.0036 1.0060 0.0000 ; −0.0043 −0.0075 1.0127]	[0.0013 0.0000 0.0000 ; 0.0024 0.0023 0.0000 ; 0.0030 0.0013 0.0023]	[0.0000 0.0000 0.0000 ; 0.0000 0.0000 0.0000 ; 0.0000 0.0000 0.0000]
Matrix_r7	[0.9885 0.0000 0.0000 ; 0.0057 0.9937 0.0000 ; −0.0068 −0.0117 1.0024]	[0.0240 0.0000 0.0000 ; 0.0001 0.0220 0.0000 ; 0.0002 0.0003 0.0221]	[0.0000 0.0000 0.0000 ; 0.0000 0.0000 0.0000 ; 0.0000 0.0000 0.0000]

Table 5: Cluster 4 FGM calibration parameters statistics over the entire mission lifetime. Offsets are expressed in nT, angles in degrees, matrix elements are adimensional factors.

parameter	mission average	mean yearly standard deviation	decadal trend
offset_r2	[1.4 1.0 1.6]	[0.0 0.0 0.0]	[0.0 0.0 0.0]
offset_r3	[1.4 1.1 1.6]	[0.0 0.0 0.0]	[0.0 0.0 0.0]
offset_r4	[9.6 7.5 9.8]	[0.1 0.1 0.1]	[0.3 0.0 0.0]
offset_r5	[10.7 9.0 10.5]	[0.3 0.1 0.1]	[0.7 0.0 0.0]
offset_r6	[97.8 76.9 97.5]	[13.7 8.3 10.4]	[0.0 0.0 0.0]
offset_r7	[161.9 135.5 160.6]	[3.8 3.1 3.4]	[0.0 0.0 0.0]
offset_sc	[−14.4 −4.3 2.7]	[0.2 0.1 0.1]	[0.3 0.0 −0.3]
Angle_xyz	[−0.0070 0.3394 0.0000]	[0.0021 0.0038 0.0000]	[−0.0108 0.0082 0.0000]
Matrix_r2	[1.0421 0.0000 −0.0003] [−0.0074 1.0794 0.0000] [0.0084 −0.0220 1.0517]	[0.0000 0.0000 0.0001] [0.0002 0.0018 0.0000] [0.0002 0.0001 0.0004]	[0.0000 0.0000 0.0000] [0.0000 0.0000 0.0000] [−0.0004 0.0002 0.0018]
Matrix_r3	[1.0235 0.0000 −0.0003] [−0.0075 1.0603 0.0000] [0.0087 −0.0215 1.0342]	[0.0000 0.0000 0.0001] [0.0001 0.0000 0.0000] [0.0002 0.0001 0.0001]	[0.0000 0.0000 0.0000] [−0.0002 0.0000 0.0000] [0.0000 0.0003 0.0000]
Matrix_r4	[1.0045 0.0000 −0.0001] [−0.0074 1.0458 0.0000] [0.0086 −0.0215 1.0178]	[0.0005 0.0000 0.0001] [0.0001 0.0004 0.0000] [0.0002 0.0001 0.0001]	[0.0000 0.0000 0.0000] [0.0000 0.0000 0.0000] [0.0000 0.0003 −0.0002]
Matrix_r5	[0.9885 0.0000 −0.0001] [−0.0078 1.0279 0.0000] [0.0086 −0.0201 1.0016]	[0.0004 0.0000 0.0001] [0.0003 0.0003 0.0000] [0.0002 0.0003 0.0001]	[0.0000 0.0000 0.0000] [0.0000 0.0000 0.0000] [0.0000 0.0000 0.0000]
Matrix_r6	[1.0054 0.0000 0.0000] [−0.0050 1.0305 0.0000] [0.0057 −0.0136 1.0145]	[0.0037 0.0000 0.0000] [0.0012 0.0116 0.0000] [0.0015 0.0020 0.0031]	[0.0000 0.0000 0.0000] [0.0000 0.0000 0.0000] [0.0000 0.0000 0.0000]
Matrix_r7	[0.9879 0.0000 0.0000] [−0.0072 1.0282 0.0000] [0.0086 −0.0211 1.0047]	[0.0275 0.0000 0.0000] [0.0002 0.0258 0.0000] [0.0002 0.0005 0.0253]	[0.0000 0.0000 0.0000] [0.0000 0.0000 0.0000] [0.0000 0.0000 0.0000]

References

Alconcel, L. N. S., Fox, P., Brown, P., Oddy, T. M., Lucek, E. L., and Carr, C. M. (2014). An initial investigation of the long-term trends in the fluxgate magnetometer (FGM) calibration parameters on the four Cluster spacecraft. *Geoscientific Instrumentation, Methods and Data Systems*, 3(2):95–109.

Auster, H. U., Fornacon, K. H., Georgescu, E., Glassmeier, K. H., and Motschmann, U. (2002). Calibration of flux-gate magnetometers using relative motion. *Measurement Science and Technology*, 13(7):1124.

Balogh, A., Dunlop, M. W., Cowley, S. W. H., Southwood, D. J., Thomlinson, J. G., Glassmeier, K. H., Musmann, G., Luhr, H., Buchert, S., Acuña, M. H., Fairfield, D. H., Slavin, J. A., Riedler, W., Schwingenschuh, K., and Kivelson, M. G. (1997). The Cluster Magnetic Field Investigation. *Space Science Reviews*, 79:65–91.

Belcher, J. W. (1973). A variation of the Davis-Smith method for in-flight determination of spacecraft magnetic fields. *J. Geophys. Res.*, 78:6480.

ESA (2013). Cluster and Double Star Science Archive. `https://cosmos.esa.int/web/csa`. Accessed: 2025-09-24.

Escoubet, C. P., Masson, A., Laakso, H., Goldstein, M. L., Dimbylow, T., Bogdanova, Y. V., Hapgood, M., Sousa, B., Sieg, D., and Taylor, M. G. G. T. (2021). Cluster After 20 Years of Operations: Science Highlights and Technical Challenges. *Journal of Geophysical Research (Space Physics)*, 126(8):e29474.

Escoubet, C. P., Schmidt, R., and Goldstein, M. L. (1997). Cluster: Science and Mission Overview. *Space Sci. Rev.*, 79:11–32.

Farrell, W. M., Thompson, R. F., Lepping, R. P., and Byrnes, J. B. (1995). A method of calibrating magnetometers on a spinning spacecraft. *IEEE Transactions on Magnetics*, 31(2):966–972.

Fornaçon, K.-H., Auster, H. U., Georgescu, E., Baumjohann, W., Glassmeier, K. H., Haerendel, G., Rustenbach, J., and Dunlop, M. (1999). The magnetic field experiment onboard Equator-S and its scientific possibilities. *Annales Geophysicae*, 17(12):1521–1527.

Fornaçon, K.-H., Georgescu, E., Kempen, R., and Constantinescu, D. (2011). Fluxgate magnetometer data processing for Cluster. Technical Report CL–IGEP–SN–0001, Institut für Geophysik und extraterrestrische Physik, Technische Universität Braunschweig, Germany.

Glassmeier, K., Richter, I., Diedrich, A., Musmann, G., Auster, U., Motschmann, U., Balogh, A., Carr, C., Cupido, E., Coates, A., Rother, M., Schwingenschuh, K., Szegö, K., and Tsurutani, B. (2007). RPC-MAG The Fluxgate Magnetometer in the ROSETTA Plasma Consortium. *Space Sci. Rev.*, 128:649–670.

Grison, B., Darrouzet, F., Maggiolo, R., Hajoš, M., Dvořák, M., Švanda, M., Jeřábková, A., Taylor, M. G. G. T., Herment, D., Masson, A., Souček, J., Santolík, O., and De Keyser, J. (2025). Localization of the Cluster satellites in the geospace environment. *Scientific Data*, 12(1):327.

Haerendel, G. (2000). EQUATOR-S: The Mission and First Coordinated Measurements with Geotail. *Advances in Space Research*, 25(7-8):1277–1286.

Hedgecock, P. C. (1975). A correlation technique for magnetometer zero level determination. *Space Science Instrumentation*, 1:83–90.

Kepko, E. L., Khurana, K. K., Kivelson, M. G., Elphic, R. C., and Russell, C. T. (1996). Accurate determination of magnetic field gradients from four point vector measurements. I. Use of natural constraints on vector data obtained from a single spinning spacecraft. *IEEE Transactions on Magnetics*, 32:377–385.

Leinweber, H. K., Russell, C. T., Torkar, K., Zhang, T. L., and Angelopoulos, V. (2008). An advanced approach to finding magnetometer zero levels in the interplanetary magnetic field. *Measurement Science and Technology*, 19(5):055104.

Plaschke, F., Auster, H.-U., Fischer, D., Fornaçon, K.-H., Magnes, W., Richter, I., Constantinescu, D., and Narita, Y. (2019). Advanced calibration of magnetometers on spin-stabilized spacecraft based on parameter decoupling. *Geoscientific Instrumentation, Methods and Data Systems*, 8(1):63–76.

Plaschke, F. and Narita, Y. (2016). On determining fluxgate magnetometer spin axis offsets from mirror mode observations. *Annales Geophysicae*, 34(9):759–766.

Primdahl, F. (1979). The fluxgate magnetometer. *Journal of Physics E: Scientific Instruments*, 12(4):241–253.

Scott, D. W. (2015). *Multivariate Density Estimation: Theory, Practice, and Visualization*. Wiley Series in Probability and Statistics. John Wiley & Sons, Inc.